

Curvature-Selective Nanocrystal Surface Ligation Using Sterically-Encumbered Metal-Coordinating Ligands

Yufei Wang,¹ Amanda A. Chen,¹ Krista P. Balto,¹ Yu Xie, Joshua S. Figueroa,* Tod A. Pascal,* and Andrea R. Tao*



Cite This: <https://doi.org/10.1021/acsnano.2c04595>



Read Online

ACCESS |

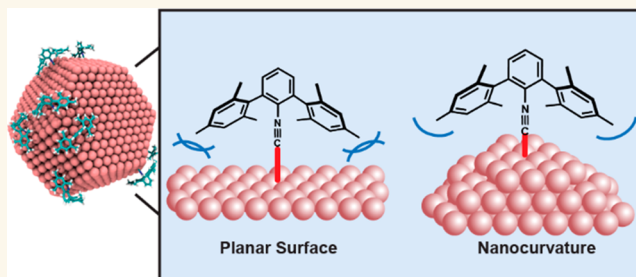
Metrics & More

Article Recommendations

Supporting Information

ABSTRACT: Organic ligands are critical in determining the physiochemical properties of inorganic nanocrystals. However, precise nanocrystal surface modification is extremely difficult to achieve. Most research focuses on finding ligands that fully passivate the nanocrystal surface, with an emphasis on the supramolecular structure generated by the ligand shell. Inspired by molecular metal-coordination complexes, we devised an approach based on ligand anchoring groups that are flanked by encumbering organic substituents and are chemoselective for binding to nanocrystal corner, edge, and facet sites. Through experiment and theory, we affirmed that the surface-ligand steric pressures generated by these organic substituents are significant enough to impede binding to regions of low nanocurvature, such as nanocrystal facets, and to promote binding to regions of high curvature such as nanocrystal edges.

KEYWORDS: Nanoparticles, surface curvature, molecular dynamics, selective binding, size-separation



Inorganic nanocrystals are bound by crystalline facets that present highly undercoordinated surface sites at the corners and edges of the nanocrystal. Chemical modification of these surface sites can have a profound effect on the distinctive properties of a nanocrystal, including its optoelectronic function,¹ catalytic reactivity,² and ability to self-assemble.^{3–5} Ligands that feature anchoring groups with favorable nanocrystal binding energies typically result in indiscriminate binding to all available surface sites, as exemplified by thiolated molecules where strong metal–sulfur bonds facilitate the formation of a molecular monolayer.⁶ Nanocrystal surface ligation is further complicated by the consideration of solvent interactions, which can significantly alter both the thermodynamics and dynamics of surface–ligand interactions and, thus, interfere with binding site selectivity. As a result, very few strategies are successful in anchoring ligands with precision to specific nanocrystal features.

In contrast, ligand-design strategies, often implemented through synthetic organic chemistry, are routinely employed to control the coordination number, geometry, and overall electronic structure of molecular transition-metal complexes.^{8–10} As a general principle, ligands featuring encumbering steric profiles can enforce and stabilize low coordination numbers for transition metal centers. A particularly effective

scaffold used in the synthesis and stabilization of reactive, low-coordinate metal centers is the *m*-terphenyl ligand class,^{11–15} in which two sterically encumbering arene groups flank a metal-binding group on a central aryl ring. This specific molecular topology places considerable steric demands in the direction pointing toward the metal primary coordination sphere and, as a result, can promote low coordination numbers in molecular complexes through ligand–ligand steric interference (Figure 1A). We reasoned that the *m*-terphenyl backbone, when attached to the surface of a nanocrystal, could serve to differentiate undercoordinated binding sites via surface–ligand steric interference. For surfaces with high nanocurvature, such as nanocrystal corners and edges, binding should result in low steric interference from neighboring surface atoms in the vicinity of ligand anchoring sites. Correspondingly, surfaces with low nanocurvature, such as nanocrystal facets, more closely approximate a planar surface where the steric pressure

Received: May 10, 2022

Accepted: July 29, 2022

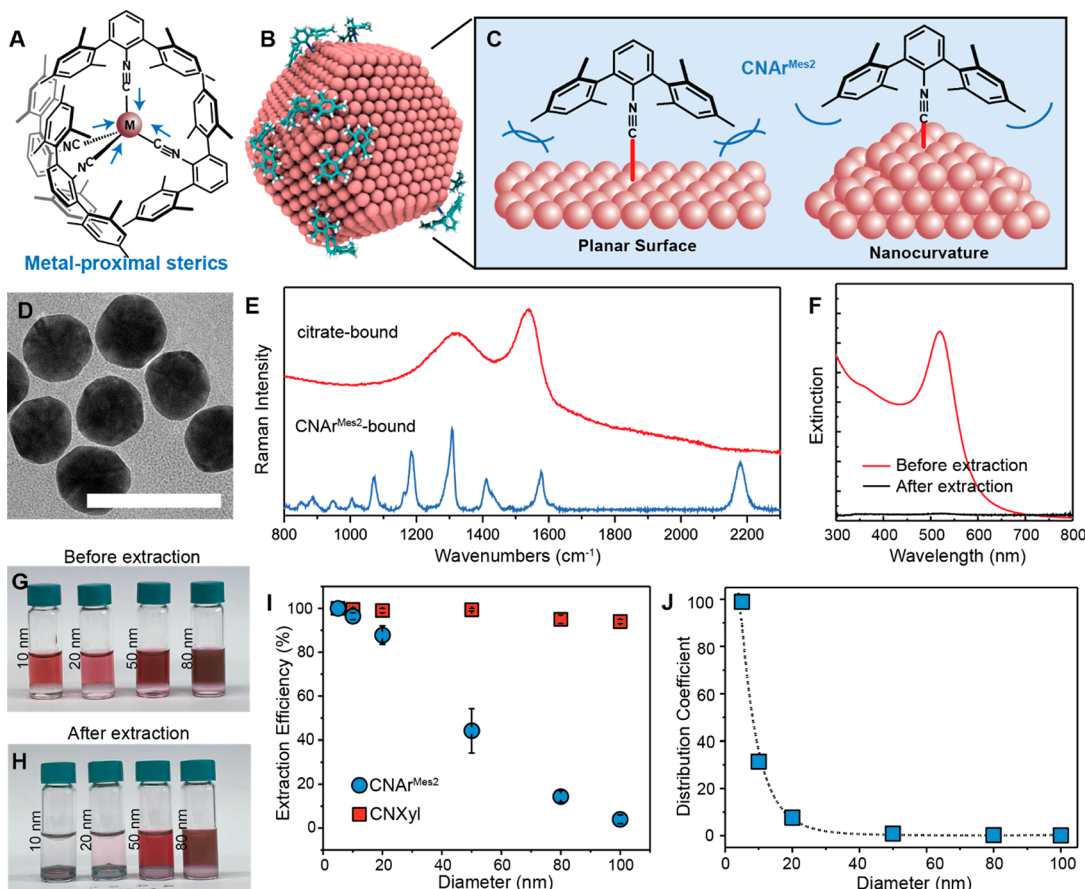


Figure 1. Nanocurvature selectivity enabled by surface-ligand steric interactions. Schematic of (A) a tetrahedral coordination complex formed by *m*-terphenyl isocyanide ligation to a metal center. (B) Computational model of *m*-terphenyl isocyanide ligands binding to an Au nanocrystal, where Au(100) and Au(111) surface facets generate planar, edge, and corner sites. (C) Schematic of *m*-terphenyl isocyanide selectivity for high-curvature surface binding sites due to the molecular topology of the ligand anchoring group. (D) TEM image of Au nanocrystals showing regions of high and low curvature. Scale bar = 100 nm. (E) Surface-enhanced Raman spectra for the AuNSs before and after ligand exchange with CNAr^{Mes2} indicating complete displacement of citrate. (F) UV-vis extinction spectra of the aqueous raffinate before and after ligand exchange showing near complete transfer of the AuNSs into the solvent phase. (G, H) Photo showing the ligand exchange and solvent transfer of AuNSs of varying diameters, where the top phase is the aqueous raffinate and the bottom phase is chloroform. (I) Plot comparing the extraction efficiencies for CNAr^{Mes2} and for the unencumbered CNXyl ligand. (J) Plot of the equilibrium distribution coefficient for extraction of the AuNSs into chloroform by CNAr^{Mes2} binding.

from neighboring surface atoms becomes more significant and potentially great enough to inhibit ligand binding. (Figure 1B,C)

Here, we demonstrate that *m*-terphenyl-based anchoring groups can discriminately bind to colloidal Au nanocrystals of varying diameter (Figure 1D) based on this concept of curvature-dependent steric pressure. We specifically employ encumbering *m*-terphenyl isocyanide ligands,^{13–15} which provide a three-atom linker between a surface Au binding atom and the central aryl ring of the *m*-terphenyl backbone. This allows the organic substituents of the *m*-terphenyl isocyanide ligands to be synthetically tuned to either maximize or relieve steric pressures across a wide degree of nanocurvature. Nanocurvature-selective ligand binding is confirmed through nanocrystal extraction experiments and is explained by atomistic modeling, employing quantum mechanical (QM) electronic-structure calculations, and molecular dynamics (MD) simulations. We conclusively demonstrate how the steric differentiation of ligand anchoring groups can be engineered, providing insights on nanocrystal ligand chemistries for improved nanocrystal synthesis and nanomanufacturing.

RESULTS/DISCUSSION

Ligand exchange reactions using pseudospherical Au nanocrystals (AuNSs) and the *m*-terphenyl isocyanide ligand CNAr^{Mes2} ($\text{Ar}^{\text{Mes2}} = 2,6\text{-}(2,4,6\text{-Me}_3\text{C}_6\text{H}_2)_2\text{C}_6\text{H}_3$)^{13,15} indicate that ligand binding is selective for nanocurvature and is consistent with ligand-surface steric interference as the dominant mechanism for selectivity. We first carried out ligand exchange of 10 nm citrate-stabilized AuNSs using the CNAr^{Mes2} ligand to facilitate nanocrystal transfer from an aqueous phase to chloroform. Importantly, unencumbered alkyl and aryl isocyanides have been well established to bind to Au surfaces and nanoparticles,^{16–22} and can exhibit surface binding energies competitive with thiols.^{19,22} Successful CNAr^{Mes2} complexation to the AuNSs was accompanied by a corresponding color change of the aqueous phase (raffinate) from red to colorless. Upon transfer into chloroform, the CNAr^{Mes2}-bound AuNSs aggregated to form a gray precipitate that was readily extracted via solvent evaporation or centrifugation. Transmission electron microscopy (TEM) images of the extracted precipitate showed well-separated AuNSs with no changes in the core nanocrystal sizes (Figure

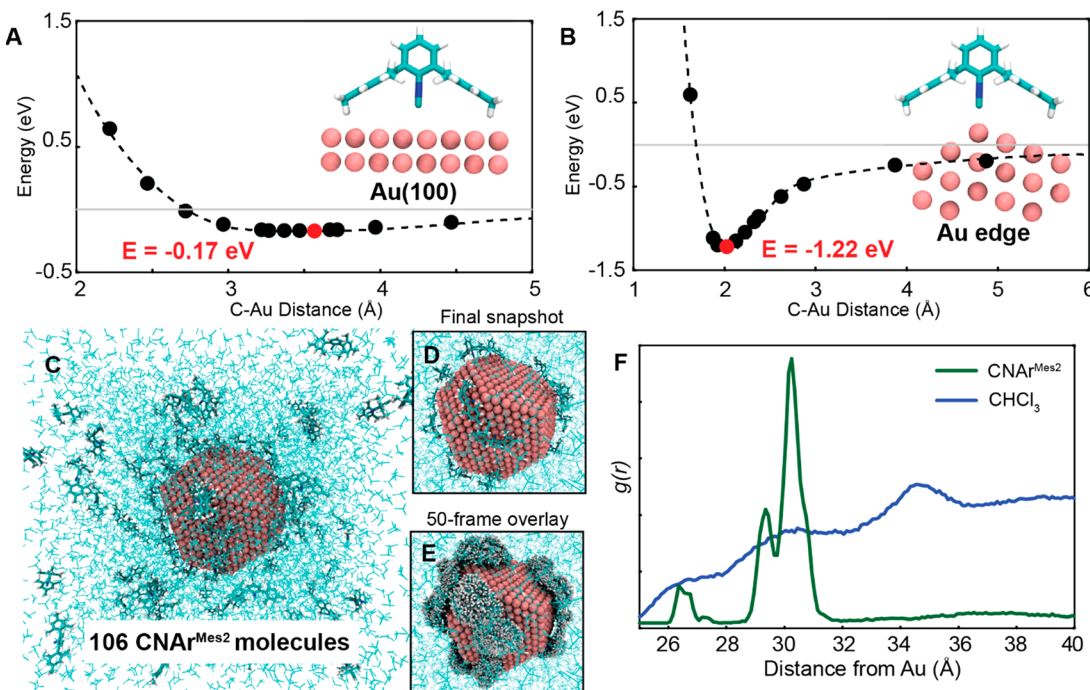


Figure 2. $\text{CNAr}^{\text{Mes}2}$ binding to Au nanocrystals. QM/DFT interaction energy plots of binding to (A) a flat Au(001) surface and (B) an Au edge site. The data (solid circles) are connected with a dashed line to guide the eye. The most favorable distance and energy are indicated in red. (Inset) atomistic model of the lowest energy configuration. (C) Final snapshot from the equilibrium MD simulation at 298 K in CHCl_3 . (D) Zoom-in of the Au nanocrystal with bound $\text{CNAr}^{\text{Mes}2}$ and (E) an overlay of the last 50 frames of the MD trajectory, illustrating edge-specific binding and diffusion. (F) Radial distribution function of $\text{CNAr}^{\text{Mes}2}$ (green) and CHCl_3 (blue) taken with the AuNS center of mass as the origin. AuNS facets are located at 21–24 Å away and AuNS edges are located at 26–27 Å away. The peaks for $\text{CNAr}^{\text{Mes}2}$ at 29–30 Å correspond to adsorbed $\text{CNAr}^{\text{Mes}2}$ at edge sites, consistent with our DFT results. The peaks for $\text{CNAr}^{\text{Mes}2}$ at <28 Å correspond to diffusive motion of $\text{CNAr}^{\text{Mes}2}$ on the AuNS surface, which results in some $\text{CNAr}^{\text{Mes}2}$ mass crossing over to the flat surface, as seen in (E).

S2 of the Supporting Information). Binding of $\text{CNAr}^{\text{Mes}2}$ was characterized by zeta potential measurements (Figure S9) and surface-enhanced Raman spectroscopy (Figure 1E), which shows complete displacement of citrate by $\text{CNAr}^{\text{Mes}2}$ and a sharp peak at 2166 cm^{-1} corresponding to the $\nu(\text{CN})$ stretching vibrations of Au-bound isocyanide.^{13,14,16,17,20,23,24} Complete transfer of the AuNSs into chloroform was confirmed by extinction measurements (Figure 1F) of the raffinate, where the optical density (OD) goes to near-zero after ligand exchange.

The metal-proximal steric properties of $\text{CNAr}^{\text{Mes}2}$ are expected to result in less favorable binding energies for larger AuNSs, for which surface curvature is lower and steric interactions begin to dominate surface-ligand interactions. Because AuNSs possess pseudospherical morphologies with irregular faceting, the surface selectivity of $\text{CNAr}^{\text{Mes}2}$ is expected to depend not only on AuNS size, but also the relative number of edge and corner sites to facet sites available for ligand adsorption, with larger AuNSs possessing a lower ratio for edge and corner sites than smaller AuNSs. To confirm this, we measured the phase transfer efficiencies for AuNSs with varying diameters, which is dictated by the ligand exchange equilibrium between citrate and $\text{CNAr}^{\text{Mes}2}$ at the water/chloroform interface (Figure 1G–I). The equilibrium distribution coefficient (D) exhibits an asymptotic decay with AuNS diameter consistent with inhibition of isocyanide binding to low-curvature Au surface sites (Figure 1J). In contrast, phase transfer using 2,6-dimethylphenyl isocyanide (CNXyl ; Xyl = 2,6- $\text{Me}_2\text{C}_6\text{H}_3$), which possesses an unencumbered isocyanide headgroup, exhibits a high exchange

efficiency for all AuNS sizes, consistent with indiscriminate Au surface binding.

To pinpoint how the molecular topology of $\text{CNAr}^{\text{Mes}2}$ leads to this curvature selectivity, we performed QM calculations employing density functional theory at the PBE/GGA level with dispersion corrections. A planar Au surface was modeled as either perfect Au(100) or Au(111) slabs, while a curved surface was modeled as an edge site at the intersection of the slabs. The binding energy was taken as the lowest energy for the closest approach of the $\text{CNAr}^{\text{Mes}2}$ ligand to each surface. We found that in vacuum, $\text{CNAr}^{\text{Mes}2}$ exhibited a larger binding energy for edge sites ($E = -1.22 \text{ eV}$) than for the Au(100) surface ($E = -0.17 \text{ eV}$) (Figure 2A,B). Closer examination shows that the steric profile of the flanking arenes on $\text{CNAr}^{\text{Mes}2}$ allows for a closer approach of the isocyanide group at the Au edge sites, with a C–Au distance of 2.0 Å. In contrast, steric interactions between these arenes and neighboring Au atoms on the Au(100) slab enforce a longer C–Au bond distance of 3.6 Å and thus weaker metal–ligand binding.

The presence of solvent modulates isocyanide ligand binding to the Au surface, as expected, and is an effect we quantify by means of extensive MD simulations. Here, we modeled a 5 nm diameter AuNS as a chamfered cube bound by Au(100) and Au(111) facets with edge lengths of 1.7 nm (Figure S12). Snapshots of the system solvated in CHCl_3 and structural analysis by means of radial distribution functions showed that $\text{CNAr}^{\text{Mes}2}$ selectively binds to the edges of the Au nanocrystal (Figure 2C–F). Our simulations also reveal that while the binding of $\text{CNAr}^{\text{Mes}2}$ to the solvated nanocrystal is strong (with no observed $\text{CNAr}^{\text{Mes}2}$ desorption), the molecules selectively

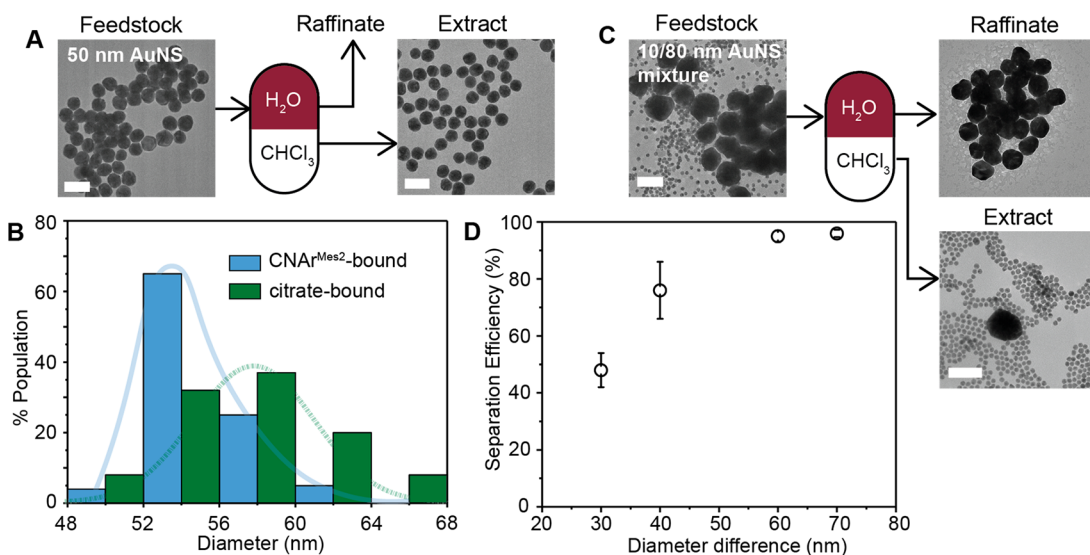


Figure 3. Size-selective LLE of AuNS dispersions. (A) TEM images of a AuNS dispersion before and after size-focusing. The final AuNS population is extracted from the chloroform phase. (B) Size distributions for an AuNS dispersion before (citrate-bound) and after (CNAr^{Mes2}-bound) size-focusing. Tick labels denote a bin size of 4 nm. (C) TEM images of AuNSs in the raffinate and extract after LLE was carried out on a binary feedstock of 10 and 80 nm citrate-coated AuNSs. (D) Plot of separation efficiencies for LLE experiments carried out with the following binary feedstocks: 10/80, 20/80, 10/50, and 20/50 nm AuNS mixtures. Scale bars = 100 nm.

diffuse along the edge sites. (Figure 2E) Along with accelerated MD simulations (Figure S14), as detailed in Supporting Information S2.6, these computational results are consistent with a predicted 150-fold increased CNAr^{Mes2} binding to the edge sites.

Microscopic insights into the ligand exchange process were also quantified using accelerated MD simulations of CNAr^{Mes2} bound to AuNSs in water. These simulations revealed that CNAr^{Mes2} binding free energies in water are reduced on the edge sites, in sharp contrast to the energetics in chloroform. We also calculated an unfavorable free energy of CNAr^{Mes2} transfer from chloroform to water based on the solvation free energies of the solvated ligand (Table S2). As a result, in a water/chloroform mixture solution, CNAr^{Mes2} favors transfer from aqueous phase into chloroform phase (Figure S16). Thus, the solvent-philic forces between CNAr^{Mes2} and chloroform are the major thermodynamic driving force for the complete transfer of CNAr^{Mes2}-bound AuNSs into the chloroform phase and our calculations support our hypothesis that it is unlikely that any CNAr^{Mes2}-bound AuNSs remain in the aqueous phase.

On the basis of these results, we used CNAr^{Mes2} to carry out liquid–liquid extraction (LLE) of AuNSs based on the observed selectivity for nanocurvature (Figure 3). Classical LLE is often used to separate molecular transition-metal complexes based on their relative solubilities, and involves transfer/partitioning of the desired isolate from liquid phases of differing polarity.²⁵ In our LLE method, AuNSs serve as the isolate and are partitioned between immiscible aqueous and chloroform phases using CNAr^{Mes2} to facilitate selective solvent transfer based on nanocrystal size. We approximated an equilibrium binding threshold for CNAr^{Mes2} at $D = 1$, corresponding to 55 nm AuNSs based on the decay fit in Figure 1J. Nanocrystal size-focusing and size-separation experiments were designed with this size threshold in mind. For size-focusing, we used a starting feedstock of citrate-capped AuNSs with an average particle diameter of 56 ± 6 nm, as obtained by TEM image analysis (Figure 3A). After LLE,

the extracted AuNSs show a significant reduction in the average diameter and distribution at 54 ± 2 nm. In addition, no AuNSs larger than 64 nm are observed in the chloroform extract, demonstrating the ability to selectively retain larger AuNSs in the aqueous raffinate (Figure 3B). For size-separation, we used an aqueous feedstock containing a mixture of two AuNS populations with different average sizes. For a 10/80 nm feedstock, TEM analysis showed that 10 nm particles were the predominant population in the chloroform extract, while 80 nm AuNSs were the exclusive population of the corresponding raffinate (Figure 3C). OD measurements indicate that 96% of the 80 nm AuNSs remain in the raffinate, which we take as the overall separation efficiency for the 10/80 nm feedstock. We also measured the separation efficiency of three additional binary feedstocks (20/80, 10/50, and 20/50 nm), with our results indicating a separation resolution of ~ 40 nm for our LLE method (Figure 3D).

We computationally screened two additional *m*-terphenyl isocyanide ligands that were expected to exhibit increased ligand-surface steric pressures: CNAr^{Dipp2} ($\text{Ar}^{\text{Dipp2}} = 2,6-(i\text{-Pr})_2\text{C}_6\text{H}_3)_2\text{C}_6\text{H}_3$; *i*-Pr = *iso*-propyl)¹⁴ and CNAr^{Tripp2} ($\text{Ar}^{\text{Tripp2}} = 2,6-(2,4,6-(i\text{-Pr})_3\text{C}_6\text{H}_2)_2\text{C}_6\text{H}_3$).¹⁵ The results for CNXyl, for which we experimentally observed uninhibited AuNS binding across all AuNS sizes, are also shown for comparison. The calculated QM interaction energies indicate that both CNAr^{Dipp2} and CNAr^{Tripp2} ligands exhibit weaker Au edge-site binding than CNAr^{Mes2}, with binding energies of -0.89 eV and -0.58 eV, respectively (Figure 4A–C). CNAr^{Dipp2}, which lacks a substituent in the *para*-position of the flanking arene ring, exhibited stronger binding to facet sites than CNAr^{Mes2}, with $E = -0.29$ eV. The more encumbering and functionalized arene groups in CNAr^{Dipp2} and CNAr^{Tripp2} also increased the oleophilicity of the ligands.

To better correlate these calculated free energies with experimental ligand exchange and LLE outcomes, we considered four computational descriptors for optimizing nanocurvature selectivity binding and solvent extraction of AuNSs using various ligand anchoring chemistries (Table S3).

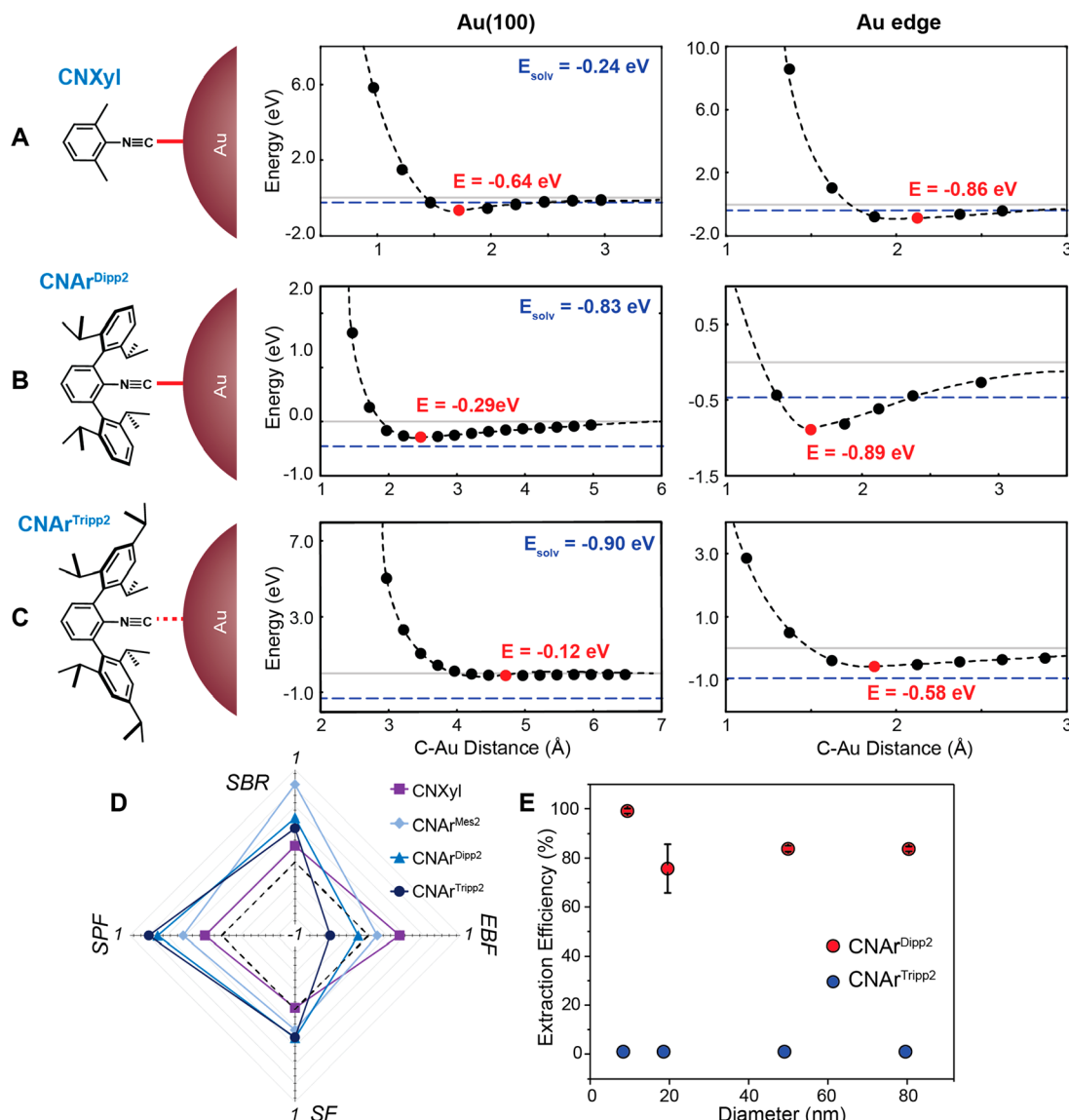


Figure 4. Surface-ligand steric pressure by design. Schematics of AuNS binding and QM/DFT interaction energy plots of binding for (A) CNXyl, (B) CNAr^{Dipp2}, and (C) CNAr^{Tripp2}, which possess organic substituents with varying degrees of bulkiness. For interaction energy plots, the data (solid circles) are connected with a dashed line to guide the eye. The most favorable distance and energy indicated in red, and solvation energies are indicated by the dashed blue line. (D) Spider plot showing site-binding ratio (SBR), edge-binding factor (EBF), solubility factor (SF), and solvent partition factor (SPF) values for CNAr^{Mes2} and the ligands in (A–C). Normalized values range from –1 to 1, with the black dashed line indicating a value of 0. (E) Experimental extraction efficiencies for CNAr^{Dipp2} and CNAr^{Tripp2} for AuNS with varying diameters. Error bars for CNAr^{Tripp2} are not shown because they are smaller than the size of the data point.

First is the site-binding ratio (SBR) calculated as the difference between the DFT interaction energies at the edge sites and a flat surface. This term describes a ligand's ability to selectively bind to high-curvature surface sites. Second is the nanocrystal edge-binding factor (EBF), calculated as the difference between the DFT interaction energy, corrected for zero-point energy and differential entropy of binding effects, at an edge site and the ligand solvation energy. This term accounts explicitly for solvent entropic effects. Third is the solubility factor (SF), calculated as the difference between the solvation free energy in chloroform and the partition factor (SPF) calculated as the difference in solvation energy of the free ligand in chloroform and cohesive free energy of the corresponding amorphous solid. This term is a thermodynamic factor related to the average concentration of the ligands located near the nanocrystal. The final descriptor is the solvent

water. This last term is related to the efficiency of the LLE process. Figure 4D plots these parameters for the *m*-terphenyl isocyanide ligands studied here, where we adopted the convention of normalized functions ranging from –1 (unfavorable) to 1 (favorable), with 0 representing the threshold value.

For CNAr^{Dipp2}, we calculated a reduced site-binding ratio of $SBR \approx 0.6$ (compared to 1.0 for CNAr^{Mes2}) and an unfavorable EBF of –0.1 (compared to 0.1 for CNAr^{Mes2}), that would preclude binding to smaller AuNSs dominated by edge and corner sites. On the other hand, the higher SPF is predicted to increase the affinity of CNAr^{Dipp2} for chloroform. LLE experiments using CNAr^{Dipp2} were consistent with our predictions, exhibiting relatively high extraction efficiencies (Figure 4E) that were particularly pronounced for larger AuNSs. In fact, we found that in this larger size regime,

CNAr^{Dipp²} outperformed CNAr^{Mes²} in facilitating AuNS LLE. The effects of steric encumbrance were even more pronounced with CNAr^{Tripp²}, where the large, negative edge-binding factor ($EBF = -0.5$) predicted unfavorable binding to nanocrystal surface sites (even regions of high curvature). Indeed, we measured extraction efficiencies of <10%, even for the smallest 10 nm AuNSs and Raman measurements indicated limited-to-no binding. Across the four isocyanide ligands studied in our experiments, tuning the steric profiles of the flanking arenes of the *m*-terphenyl group provides only moderate differentiation of ligation via SPF and SF, with all ligands providing sufficient solubility for nanocrystal postprocessing.

CONCLUSIONS

Combined, our experimental and computational results demonstrate that the steric profile of *m*-terphenyl isocyanides can enable nanocurvature-dependent binding on Au nanocrystal surfaces. We demonstrate that it is the molecular topology of the ligand anchoring group, rather than the ligand coronas, that is responsible for selective isocyanide ligation to edge and corner sites. Articulation of the ligand design principles developed in this work can now be expanded to a vast library of ligands that have already been studied for molecular metal coordination complexes. Importantly, we also find that for colloidal nanocrystals, solvent plays a critical role in not only dictating whether this steric differentiation occurs during the ligand exchange process, but also in determining the dynamics of ligand diffusion, molecular desorption, and solvent extraction after ligand exchange has occurred. Molecular topology of nanocrystal ligands must be codesigned for surface site selectivity and solubility. That solvent is capable of fine-tuning ligand–surface interactions perhaps explains why precise nanocrystal surface modification is so difficult to achieve in practice, given that it is only recently that computational approaches have been accurate and efficient enough to obtain microscopic insights into binding, thereby predicting the outcomes of these many-body, complex systems.

METHODS

Ligand Synthesis. The *m*-terphenyl isocyanide ligands CNAr^{Mes²} ($\text{Ar}^{\text{Mes}^2} = 2,6-(2,4,6-\text{Me}_3\text{C}_6\text{H}_2)_2\text{C}_6\text{H}_3$),¹³ CNAr^{Dipp²} ($\text{Ar}^{\text{Dipp}^2} = 2,6-(2,6-(i\text{-Pr})_2\text{C}_6\text{H}_3)_2\text{C}_6\text{H}_3$); *i*-Pr = iso-propyl),¹⁴ and CNAr^{Tripp²} ($\text{Ar}^{\text{Tripp}^2} = 2,6-(2,4,6-(i\text{-Pr})_3\text{C}_6\text{H}_2)_2\text{C}_6\text{H}_3$)¹⁵ were prepared as previously described.

Gold Nanospheres (AuNS) Synthesis. Citrate-AuNSs with a diameter of 5 ± 0.7 nm were purchased from *nanoComposix Inc.* of San Diego, California. Citrate-AuNSs 10 nm in diameter were synthesized according to the method of Bastús et al.²⁶ Citrate-AuNSs of 20 nm in diameter were synthesized in a modified Turkevich method.²⁷ The 20 nm AuNSs were used as-synthesized as seed particles to synthesize AuNSs of 50 nm in diameter. Briefly, an aqueous solution of the seed particles (20 nm AuNPs, 3.0 mL) and NH₂OH-HCl (200 μ L, 0.2 M) were added to 50 mL water in a 100 mL round-bottom flask. HAuCl₄·3H₂O (3.0 mL of 0.1 wt % solution in H₂O) was added dropwise to the solution under vigorous stirring and allowed to react for 30 min at room temperature. The AuNSs of 80 and 100 nm diameter were synthesized by the same seeded-growth method as the 50 nm particles. For AuNSs of 80 nm diameter, 2.0 mL seed solution was used, whereas 1.0 mL of seed solution was used to prepare AuNSs of 100 nm diameter. Additional details can be found in the Supporting Information.

Liquid–Liquid Extraction (LLE) of AuNS with Isocyanide Ligands. An aqueous dispersion of AuNSs (3.0 mL, 10^{16} atoms/mL) was layered onto a chloroform solution containing isocyanide (1.0 mL, 15 mM) in a glass vial. After layering the aqueous AuNSs

dispersion onto the organic solution, the two-phase system was mixed vigorously by hand for 30 min. The aqueous layer was decanted, and the red-colored organic phase was washed with chloroform to remove excess free ligand in solution via centrifugation. The concentration of isocyanide was optimized by evaluating the extraction efficiency (Supporting Information S1.2.) of 20 nm AuNSs functionalized with CNAr^{Mes²} and found to be 10 mM (Figure S11). To guarantee successful ligand exchange, the concentration of isocyanide used in the LLE process was increased to 15 mM.

Nanocrystal Characterization. Transmission electron microscopy (TEM) images were collected using a ThermoFisher Talos 200X TEM with an operation voltage of 200 kV. Samples were prepared by drop-casting AuNP solutions on copper grids and allowed to settle overnight in closed vials (Figure S2). UV–visible absorption measurements were performed on Cary 50/60 UV–vis spectrophotometer. Raman measurements were performed on Renishaw micro-Raman spectrometer (Renishaw Invia) coupled with a Leica microscope with 50 \times objective (Leica N-plan) in the range of 800–2400 cm⁻¹. A wavelength of 532 nm was used as an excitation source generated by 50 mW Ar-Ion LASER. Zeta potential values were measured using a Malvern NANO-ZS90 Zetasizer.

QM and MD Methods. Both quantum mechanics (QM) calculations and molecular dynamics (MD) simulations were used to study the binding thermodynamics and kinetics of the various ligands to the Au nanosphere surfaces. QM calculations were performed using the Q-Chem 5.2,²⁸ and Quantum Espresso (QE)^{29,30} electronic structure packages to determine the optimized ligand structure and the ligand–gold interaction energies, respectively. The MD simulations were performed with LAMMPS³¹ simulation engine. In MD, the Au nanoparticles were described using EAM/Fs potential of Ackland et al.³² Ligands were described using either the GAFF³³ or OPLS/AA³⁴ force fields, except for the critical C≡N bond stretching and the aromatic rings torsions, which were determined from QM to reproduce the CNXyl and CNAr^{Mes²} intramolecular motion. The CHCl₃ solvent was modeled using the Kamath et al. force field,³⁵ while the SPC/E potential was used for water.³⁶ Additional details can be found in the Supporting Information.

Computation of Normalized Descriptors. To straightforwardly compare the binding and solvation energies, DFT interaction energies were corrected for zero-point energy (ZPE) and entropy of binding (TΔS) effects:

$$\Delta G_{DFT-bind} = \Delta E_{DFT-bind} + \Delta ZPE + T\Delta S \quad (1)$$

where the ΔZPE is obtained from vibrational frequency calculations of the isolated and bound isocyanides, and $T\Delta S$ is taken as difference between the free (ideal gas) and bound isocyanides. Generally, it was found that these corrections account for $\sim+0.2$ eV for the various structures.

For the various descriptors (X), relative energies (ΔY) were calculated and divided by the norm of the largest value if it exceeds 1:

$$X = \frac{\Delta Y}{\max|\Delta Y|} \quad (2)$$

The various descriptors thus range from -1 (unfavorable) to +1 (favorable), with a favorable/unfavorable threshold taken as 0:

$$\begin{aligned} SBR &= \Delta G_{DFT-bind}^{\text{flat}} - \Delta G_{DFT-bind}^{\text{edge}} \\ EBF &= \Delta G_{DFT-bind}^{\text{edge}} - \Delta G_{\text{solvation}}^{\text{CHCl}_3} \\ SF &= \Delta G_{\text{cohesive}} - \Delta G_{\text{solvation}}^{\text{CHCl}_3} \\ SPF &= \Delta G_{\text{solvation}}^{\text{H}_2\text{O}} - \Delta G_{\text{solvation}}^{\text{CHCl}_3} \end{aligned} \quad (3)$$

where SBR is site binding ratio, EBF is edge-binding factor, SF is solubility factor, and SPF is solvent partition factor.

ASSOCIATED CONTENT

SI Supporting Information

The Supporting Information is available free of charge at <https://pubs.acs.org/doi/10.1021/acsnano.2c04595>.

Summary of description in Materials/Methods and Computational Details; figures/images of TEM, UV-vis, zeta potential, SERS, simulation model structure, simulated C≡N vibrational spectrum of CNAr^{Mes₂}, and tables of C≡N vibrational frequency, solvation free energy, computational descriptors, composition of simulation models ([PDF](#))

AUTHOR INFORMATION

Corresponding Authors

Joshua S. Figueroa — *Materials Science and Engineering Program and Department of Chemistry and Biochemistry, University of California San Diego, La Jolla, California 92023, United States;*  orcid.org/0000-0003-2099-5984; Email: jfig@ucsd.edu

Tod A. Pascal — *Department of Nanoengineering and Chemical Engineering, University of California San Diego, La Jolla, California 92023-0448, United States; Materials Science and Engineering Program, University of California San Diego, La Jolla, California 92023, United States;*  orcid.org/0000-0003-2096-1143; Email: tpascal@ucsd.edu

Andrea R. Tao — *Department of Nanoengineering and Chemical Engineering, University of California San Diego, La Jolla, California 92023-0448, United States; Materials Science and Engineering Program and Department of Chemistry and Biochemistry, University of California San Diego, La Jolla, California 92023, United States;*  orcid.org/0000-0003-1857-8743; Email: atao@eng.ucsd.edu

Authors

Yufei Wang — *Department of Nanoengineering and Chemical Engineering, University of California San Diego, La Jolla, California 92023-0448, United States; Materials Science and Engineering Program, University of California San Diego, La Jolla, California 92023, United States*

Amanda A. Chen — *Department of Nanoengineering and Chemical Engineering, University of California San Diego, La Jolla, California 92023-0448, United States;*  orcid.org/0000-0002-7358-222X

Krista P. Balto — *Department of Chemistry and Biochemistry, University of California San Diego, La Jolla, California 92023, United States;*  orcid.org/0000-0001-7526-4885

Yu Xie — *Department of Nanoengineering and Chemical Engineering, University of California San Diego, La Jolla, California 92023-0448, United States*

Complete contact information is available at:
<https://pubs.acs.org/doi/10.1021/acsnano.2c04595>

Author Contributions

[†]Y.W., A.A.C., and K.P.B. contributed equally to this work. Conceptualization: J.S.F., T.A.P., and A.R.T. Methodology: Y.W., A.A.C., K.P.B., J.S.F., T.A.P., and A.R.T. Investigation: Y.W., A.A.C., K.P.B., and Y.X. Visualization: Y.W., A.A.C., T.A.P., and A.R.T. Funding acquisition: A.R.T. Project administration: J.S.F., T.A.P., and A.R.T. Supervision: J.S.F., T.A.P., and A.R.T. Writing—original draft: J.S.F., T.A.P., and

A.R.T. Writing—review and editing: Y.W., A.A.C., K.P.B., J.S.F., T.A.P., and A.R.T.

Notes

The authors declare no competing financial interest.

ACKNOWLEDGMENTS

The authors acknowledge the use of facilities and instrumentation supported by National Science Foundation through the UC San Diego Materials Research Science and Engineering Center (UCSD MRSEC) with Grant No. DMR-2011924 and the San Diego Nanotechnology Infrastructure (SDNI) of UCSD, a member of the National Nanotechnology Coordinated Infrastructure, which is supported by the Grant ECCS-2025752. We thank the National Science Foundation, UCSD MRSEC DMR-2011924 for financial support.

REFERENCES

- (1) Kovalenko, M. V.; Scheele, M.; Talapin, D. V. Colloidal Nanocrystals with Molecular Metal Chalcogenide Surface Ligands. *Science* **2009**, *324* (5933), 1417–1420.
- (2) Kim, B. H.; Heo, J.; Kim, S.; Reboul, C. F.; Chun, H.; Kang, D.; Bae, H.; Hyun, H.; Lim, J.; Lee, H.; Han, B.; Hyeon, T.; Alivisatos, A. P.; Ercius, P.; Elmlund, H.; Park, J. Critical differences in 3D atomic structure of individual ligand-protected nanocrystals in solution. *Science* **2020**, *368* (6486), 60–67.
- (3) Yi, C.; Liu, H.; Zhang, S.; Yang, Y.; Zhang, Y.; Lu, Z.; Kumacheva, E.; Nie, Z. Self-limiting directional nanoparticle bonding governed by reaction stoichiometry. *Science* **2020**, *369* (6509), 1369–1374.
- (4) Nagaoka, Y.; Tan, R.; Li, R.; Zhu, H.; Eggert, D.; Wu, Y. A.; Liu, Y.; Wang, Z.; Chen, O. Superstructures generated from truncated tetrahedral quantum dots. *Nature* **2018**, *561* (7723), 378–382.
- (5) Santos, P. J.; Gabrys, P. A.; Zornberg, L. Z.; Lee, M. S.; Macfarlane, R. J. Macroscopic materials assembled from nanoparticle superlattices. *Nature* **2021**, *591* (7851), 586–591.
- (6) Villarreal, E.; Li, G. G.; Zhang, Q.; Fu, X.; Wang, H. Nanoscale Surface Curvature Effects on Ligand–Nanoparticle Interactions: A Plasmon-Enhanced Spectroscopic Study of Thiolated Ligand Adsorption, Desorption, and Exchange on Gold Nanoparticles. *Nano Lett.* **2017**, *17* (7), 4443–4452.
- (7) Anderson, N. C.; Chen, P. E.; Buckley, A. K.; De Roo, J.; Owen, J. S. Stereoelectronic Effects on the Binding of Neutral Lewis Bases to CdSe Nanocrystals. *J. Am. Chem. Soc.* **2018**, *140* (23), 7199–7205.
- (8) Power, P. P. Some highlights from the development and use of bulky monodentate ligands. *J. Organomet. Chem.* **2004**, *689* (24), 3904–3919.
- (9) Power, P. P. Stable Two-Coordinate, Open-Shell (d1–d9) Transition Metal Complexes. *Chem. Rev.* **2012**, *112* (6), 3482–3507.
- (10) Rivard, E.; Power, P. P. Multiple Bonding in Heavier Element Compounds Stabilized by Bulky Terphenyl Ligands. *Inorg. Chem.* **2007**, *46* (24), 10047–10064.
- (11) Clyburne, J. A. C.; McMullen, N. Unusual structures of main group organometallic compounds containing m-terphenyl ligands. *Coord. Chem. Rev.* **2000**, *210* (1), 73–99.
- (12) Kays, D. L. The stabilisation of organometallic complexes using m-terphenyl ligands. In *In Organomet. Chem.*; Royal Society of Chemistry: Cambridge, 2010; Vol. 36, pp 56–76.
- (13) Fox, B. J.; Sun, Q. Y.; Dipasquale, A. G.; Fox, A. R.; Rheingold, A. L.; Figueroa, J. S. Solution behavior and structural properties of Cu(I) complexes featuring m-terphenyl isocyanides. *Inorg. Chem.* **2008**, *47* (19), 9010–9020.
- (14) Ditri, T.; Fox, B.; Moore, C.; Rheingold, A.; Figueroa, J. Effective Control of Ligation and Geometric Isomerism: Direct Comparison of Steric Properties Associated with Bis-mesityl and Bis-diisopropylphenyl m-Terphenyl Isocyanides. *Inorg. Chem.* **2009**, *48* (17), 8362–8375.

- (15) Carpenter, A. E.; Mokhtarzadeh, C. C.; Ripatti, D. S.; Havrylyuk, I.; Kamezawa, R.; Moore, C. E.; Rheingold, A. L.; Figueroa, J. S. Comparative Measure of the Electronic Influence of Highly Substituted Aryl Isocyanides. *Inorg. Chem.* **2015**, *54* (6), 2936–2944.
- (16) Robertson, M. J.; Angelici, R. J. Adsorption of Aryl and Alkyl Isocyanides on Powdered Gold. *Langmuir* **1994**, *10* (5), 1488–1492.
- (17) Shih, K.-C.; Angelici, R. J. Equilibrium and Saturation Coverage Studies of Alkyl and Aryl Isocyanides on Powdered Gold. *Langmuir* **1995**, *11* (7), 2539–2546.
- (18) Ontko, A. C.; Angelici, R. J. Effects of Alkyl Chain Length on the Adsorption of n-Alkyl Isocyanides ($RN:C$) on Gold Powder. *Langmuir* **1998**, *14* (7), 1684–1691.
- (19) Martin, B. R.; Dermody, D. J.; Reiss, B. D.; Fang, M.; Lyon, L. A.; Natan, M. J.; Mallouk, T. E. Orthogonal Self-Assembly on Colloidal Gold-Platinum Nanorods. *Adv. Mater.* **1999**, *11* (12), 1021–1025.
- (20) Henderson, J. I.; Feng, S.; Bein, T.; Kubiak, C. P. Adsorption of Diisocyanides on Gold. *Langmuir* **2000**, *16* (15), 6183–6187.
- (21) Bae, S. J.; Lee, C.-r.; Choi, I. S.; Hwang, C.-S.; Gong, M.-s.; Kim, K.; Joo, S.-W. Adsorption of 4-Biphenylisocyanide on Gold and Silver Nanoparticle Surfaces: Surface-Enhanced Raman Scattering Study. *J. Phys. Chem. B* **2002**, *106* (28), 7076–7080.
- (22) Ahn, J.; Shi, S.; Vannatter, B.; Qin, D. Comparative Study of the Adsorption of Thiol and Isocyanide Molecules on a Silver Surface by In Situ Surface-Enhanced Raman Scattering. *J. Phys. Chem. C* **2019**, *123* (35), 21571–21580.
- (23) Arroyave, A.; Gembicky, M.; Rheingold, A. L.; Figueroa, J. S. Aqueous Stability and Ligand Substitution of a Layered Cu(I)/Isocyanide-Based Organometallic Network Material with a Well-Defined Channel Structure. *Inorg. Chem.* **2020**, *59* (17), 11868–11878.
- (24) Balto, K. P.; Gembicky, M.; Rheingold, A. L.; Figueroa, J. S. Crystalline Hydrogen-Bonding Networks and Mixed-Metal Framework Materials Enabled by an Electronically Differentiated Heteroditopic Isocyanide/Carboxylate Linker Group. *Inorg. Chem.* **2021**, *60* (16), 12545–12554.
- (25) Yang, J.; Lee, J. Y.; Ying, J. Y. Phase transfer and its applications in nanotechnology. *Chem. Soc. Rev.* **2011**, *40* (3), 1672–96.
- (26) Bastús, N. G.; Comenge, J.; Puntes, V. Kinetically controlled seeded growth synthesis of citrate-stabilized gold nanoparticles of up to 200 nm: size focusing versus Ostwald ripening. *Langmuir* **2011**, *27* (17), 11098–11105.
- (27) Kimling, J.; Maier, M.; Okenve, B.; Kotaidis, V.; Ballot, H.; Plech, A. Turkevich method for gold nanoparticle synthesis revisited. *J. Phys. Chem. B* **2006**, *110* (32), 15700–15707.
- (28) Shao, Y.; Gan, Z.; Epifanovsky, E.; Gilbert, A. T.; Wormit, M.; Kussmann, J.; Lange, A. W.; Behn, A.; Deng, J.; Feng, X.; et al. Advances in molecular quantum chemistry contained in the Q-Chem 4 program package. *Mol. Phys.* **2015**, *113*, 184–215.
- (29) Giannozzi, P.; Baroni, S.; Bonini, N.; Calandra, M.; Car, R.; Cavazzoni, C.; Ceresoli, D.; Chiarotti, G. L.; Cococcioni, M.; Dabo, I.; Corso, A. D.; Gironcoli, S. d.; Fabris, S.; Fratesi, G.; Gebauer, R.; Gerstmann, U.; Gougoussis, C.; Kokalj, A.; Lazzeri, M.; Martin-Samos, L.; Marzari, N.; Mauri, F.; Mazzarello, R.; Paolini, S.; Pasquarello, A.; Paulatto, L.; Sbraccia, C.; Scandolo, S.; Sclauzero, G.; Seitsonen, A. P.; Smogunov, A.; Umari, P.; Wentzcovitch, R. M. QUANTUM ESPRESSO: a modular and open-source software project for quantum simulations of materials. *J. Phys.: Condens. Matter* **2009**, *21*, 395502.
- (30) Giannozzi, P.; Andreussi, O.; Brumme, T.; Bunau, O.; Nardelli, M. B.; Calandra, M.; Car, R.; Cavazzoni, C.; Ceresoli, D.; Cococcioni, M.; Colonna, N.; Carnimeo, I.; Corso, A. D.; Gironcoli, S. d.; Delugas, P.; Floris, R.; Fratesi, G.; Fugallo, G.; Gebauer, R.; Gerstmann, U.; Giustino, F.; Gorni, T.; Jia, J.; Kawamura, M.; Ko, H.-Y.; Kokalj, A.; Küçükbenli, E.; Lazzeri, M.; Marsili, M.; Marzari, N.; Mauri, F.; Nguyen, N. L.; Nguyen, H.-V.; Otero-de-la-Roza, A.; Paulatto, L.; Poncé, S.; Rocca, D.; Sabatini, R.; Santra, B.; Schlipf, M.; Seitsonen, A. P.; Smogunov, A.; Timrov, I.; Thonhauser, T.; Umari, P.; Vast, N.; Wu, X.; Baroni, S. Advanced capabilities for materials modelling with Quantum ESPRESSO. *J. Phys.: Condens. Matter* **2017**, *29*, 465901.
- (31) Plimpton, S. Fast Parallel Algorithms for Short-Range Molecular Dynamics. *J. Comput. Phys.* **1995**, *117*, 1–19.
- (32) Ackland, G. J.; Tichy, G.; Vitek, V.; Finnis, M. W. Simple N-body potentials for the noble metals and nickel. *Philosophical Magazine A* **1987**, *56* (6), 735–756.
- (33) Wang, J.; Wolf, R. M.; Caldwell, J. W.; Kollman, P. A.; Case, D. A. Development and testing of a general amber force field. *J. Comput. Chem.* **2004**, *25* (9), 1157–74.
- (34) Kaminski, G. A.; Friesner, R. A.; Tirado-Rives, J.; Jorgensen, W. L. Evaluation and reparametrization of the OPLS-AA force field for proteins via comparison with accurate quantum chemical calculations on peptides. *J. Phys. Chem. B* **2001**, *105* (28), 6474–6487.
- (35) Kamath, G.; Georgiev, G.; Potoff, J. J. Molecular Modeling of Phase Behavior and Microstructure of Acetone-Chloroform-Methanol Binary Mixtures. *J. Phys. Chem. B* **2005**, *109*, 19463–19473.
- (36) Mark, P.; Nilsson, L. Structure and Dynamics of the TIP3P, SPC, and SPC/E Water Models at 298 K. *J. Phys. Chem. A* **2001**, *105*, 9954–9960.